Seismicity induced by seasonal groundwater recharge at Mt. Hood, Oregon

Martin O. Saar [a,b,*], Michael Manga [a,b]

[a] *Department of Earth and Planetary Science, University of California, Berkeley, CA, USA*
[b] *Earth Sciences Division, Lawrence Berkeley National Laboratory, Berkeley, CA, USA*

Abstract

Groundwater recharge at Mt. Hood, Oregon, is dominated by spring snow melt which provides a natural large-amplitude and narrow-width pore-fluid pressure signal. Time delays between this seasonal groundwater recharge and seismicity triggered by groundwater recharge can thus be used to estimate large-scale hydraulic diffusivities and the state of stress in the crust. We approximate seasonal variations in groundwater recharge with discharge in runoff-dominated streams at high elevations. We interpolate the time series of number of earthquakes, N, seismic moment, M_o, and stream discharge, Q, and determine cross-correlation coefficients at equivalent frequency bands between Q and both N and M_o. We find statistically significant correlation coefficients at a mean time lag of about 151 days. This time lag and a mean earthquake depth of about 4.5 km are used in the solution to the pressure diffusion equation, under periodic (1 year) boundary conditions, to estimate a hydraulic diffusivity of $\kappa \approx 10^{-1}$ m^2/s, a hydraulic conductivity of about $K_h \approx 10^{-7}$ m/s, and a permeability of about $k \approx 10^{-15}$ m^2. Periodic boundary conditions also allow us to determine a critical pore-fluid pressure fraction, $P'/P_0 \approx 0.1$, of the applied near-surface pore-fluid pressure perturbation, $P_0 \approx 0.1$ MPa, that has to be reached at the mean earthquake depth to cause hydroseismicity. The low magnitude of $P' \approx 0.01$ MPa is consistent with other studies that propose $0.01 \leq P' \leq 0.1$ MPa and suggests that the state of stress in the crust near Mt. Hood could be near critical for failure. Therefore, we conclude that, while earthquakes occur throughout the year at Mt. Hood, elevated seismicity levels along pre-existing faults south of Mt. Hood during summer months are hydrologically induced by a reduction in effective stress.
© 2003 Elsevier B.V. All rights reserved.

1. Introduction

Natural or artificial changes in pore-fluid pres-

sure may trigger earthquakes, a process hereafter referred to as hydroseismicity. Examples include hydroseismicity induced by reservoirs [1–3], by fluid injection into [4–8] or withdrawal from [9–11] aquifers or oil reservoirs, or by pore-fluid pressure changes induced by other earthquakes [12,13]. It has also been suggested that hydroseismicity may be caused by changes in groundwater

---

* Corresponding author. Tel.: +1-510-643-5450;
Fax: +1-510-643-9980.
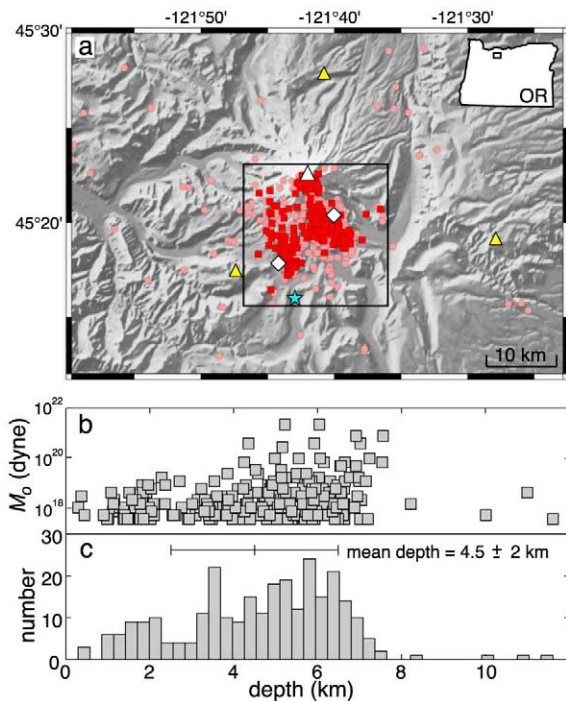 *E-mail address:* saar@eps.berkeley.edu (M.O. Saar).

Fig. 1. (a) Shaded relief map of Mt. Hood, Oregon, indicating all earthquakes (pink circles and red squares) and selected (for criteria see text) earthquakes (red squares), stream discharge gauging station on Salmon River (blue star), summit of Mt. Hood (large white triangle), and hydrothermal Swim Warm Springs (western white diamond) and Meadows Spring (eastern white diamond). Three (small yellow triangles) out of 14 relevant seismometers (Appendix A) are located within the map region. (b) Seismic moment, M_o, versus earthquake depth. (c) Histogram of earthquake depths, mean earthquake depth (4.5 km), and range of 1σ standard deviation (2 km).

recharge rates [14–16] which can be the result of seasonal snow melt or variations in precipitation [16–19]. In this paper we use signal processing techniques to investigate whether natural groundwater recharge variations trigger some earthquakes in the Cascade volcanic arc, USA.

The Cascade arc is located on a tectonically active, and in parts densely populated, convergent plate boundary. Thus, for both seismic and volcanic hazard assessment it is important to discern triggers of earthquakes as tectonic, magmatic, or hydrologic. Moreover, rapid groundwater recharge may initiate larger (local magnitude, $M_l > 3$) earthquakes on critically stressed faults

[20]. More generally, understanding the causes of hydroseismicity may provide additional insight into seismic hazards associated with reservoir impoundment or injection of fluids into the subsurface for example during waste fluid injection, carbon sequestration, and geothermal energy exploration. Detection of natural groundwater-recharge-induced earthquakes also provides a baseline against which reservoir- or fluid-injection-induced seismicity can be measured to evaluate the actual extent of human-caused hydroseismicity. Moreover, natural hydrologic triggering of earthquakes provides insight into the state of stress in the crust. In addition to tectonic information, the time lag between groundwater recharge and earthquakes allows us to determine hydraulic properties of the upper crust on spatial and temporal scales that are relevant for studies of regional hydrogeology.

Fig. 1a shows seismicity at Mt. Hood, Oregon, a Quaternary stratovolcano, for the period from February 4, 1980 through July 11, 2002. Earthquakes occur preferentially on the southern flanks of the volcano. The off-axis concentration suggests the possibility that earthquakes are not all
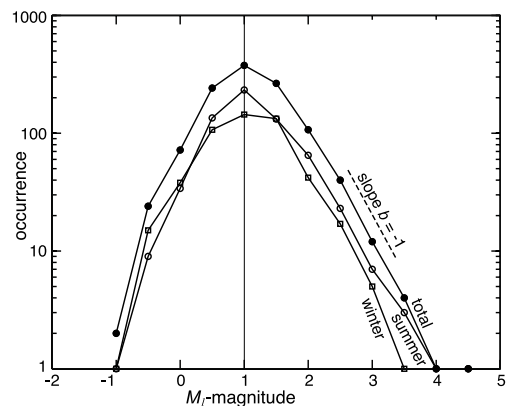

Fig. 2. Earthquake magnitude, M_l, binned in half-magnitude increments, versus logarithmic frequency of occurrence (Gutenberg–Richter relationship) for all earthquakes displayed in Fig. 1. Open circles, squares, and solid circles indicate seismicity during the summer ($15 \leq$ week ≤ 40, open circles) and winter (week ≥ 41 or week ≤ 14, open squares), and total years, respectively. Above the cut-off magnitude of $M_l = 1$ the decrease in seismicity with increasing magnitude follows approximately the expected slope of $b = -1$. This suggests that the data set is complete for $M_l \geq 1$.

caused directly by magma flow although off-centered magma-related seismicity can occur when volcanic conduits are inclined. Instead, we hypothesize that at least some seismicity could be triggered by seasonal groundwater recharge that changes pore-fluid pressures on pre-existing critically stressed faults. We select a region of concentrated off-axis seismicity (large open square in Fig. 1a) to test this hypothesis.

2. Data and analysis

The 1980 Mount St. Helens eruption increased monitoring efforts at volcanoes in the Cascade Range. As a result, the Pacific Northwest Seismic Network has maintained short-period vertical-motion seismometers around Mt. Hood since the mid-1980s (Appendix A). To reduce instrumentation bias we only use earthquakes with a minimum local magnitude of $M_l = 1$ (Fig. 2), above which $b \approx -1$ holds in the Gutenberg–Richter [24] relationship:

$$\log_{10} N = a + b M_l \tag{1}$$

where N is the number of earthquakes of magnitude M_l and a is the production of seismicity.

Seismic moment, M_o, is approximated by [24]:

$$M_o = 10^{1.5(M_w + 10.73)} \tag{2}$$

where we assume $M_w \approx M_l$ due to our small earthquake magnitudes of $M_l \le 4.5$.

Groundwater recharge at Mt. Hood is largely due to spring snow melt which provides a natural pore-fluid pressure signal of narrow temporal width and potentially relatively large amplitude. Groundwater recharge may be approximated by hydrographs of surface-runoff-dominated streams at high elevations, such as Salmon River, that show a peak in discharge during snow melt [22] (Fig. 3). Groundwater recharge may be delayed from stream discharge due to flow in the unsaturated zone. This possible delay is not considered here but may be neglected considering the uncertainty in earthquake depth discussed later.

Salmon River at USGS gauge 14134000 (blue star in Fig. 1) has a 21 km^2 drainage area. Gauge elevation is 1050 m. Stream discharge for Salmon River is only available through September 30, 1995. Thus, we determine a transfer function between stream discharge of Hood River (USGS gauge 14120000) and Salmon River using a Box–Jenkins [23] method (Appendix B). Dis-
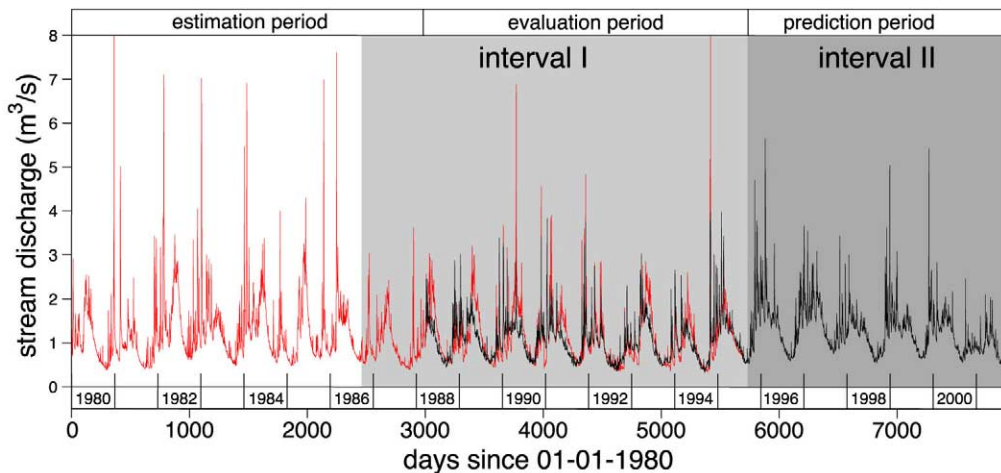

Fig. 3. Stream discharge of Salmon River, Oregon, measured at USGS gauging station 14134000 (red curve) located at an elevation of 1050 m. During the estimation period, a transfer function between Hood River and Salmon River is determined using a Box–Jenkins [23] method (Appendix B). The evaluation period shows the fit between predicted (black) and actual (red) data. The prediction period shows the estimated discharge for Salmon River. Intervals I and I+II are used in the analysis and are discussed in the main text.

charge at Hood River is available until September 30, 2001 and is convolved with the transfer function to extend the discharge data to that date (Fig. 3).

For this analysis we distinguish two time intervals. Interval I has a lower bound on October 1, 1986, i.e., at the beginning of the water year when most seismometers had been installed. The upper bound of interval I is set to the last available discharge date for Salmon River, September 30, 1995. Interval II starts on October 1, 1995 and ends when discharge measurements at Hood River were discontinued on September 30, 2001 (Fig. 3). Therefore, our analysis focuses on interval I, to allow evaluation of the best-constrained data, and on the combined interval I+II, to investigate the longest possible time series.

Fig. 4a,b shows histograms for stream discharge, Q, number of earthquakes, N, and seismic moment, M_o, binned monthly for intervals I and I+II, respectively. Elevated levels of stream discharge exist from November through June with a peak in May due to snow melt. Number of earthquakes and total seismic moment show a peak during September and October for both intervals I and I+II. In addition, interval I+II shows seismicity in January and February. For interval I, the time lag between peak stream discharge, a proxy for groundwater recharge, and seismicity is about 5 months. To test whether Q,
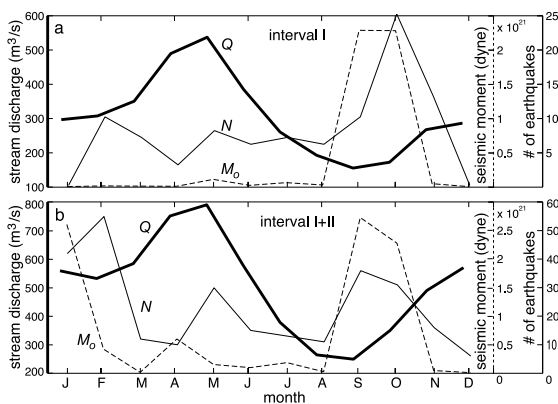

Fig. 4. Monthly binned histograms showing cumulative mean daily stream discharge (bold solid line), cumulative number of earthquakes (thin solid line), and cumulative seismic moment (thin dashed line) for (a) interval I and (b) interval I+II.
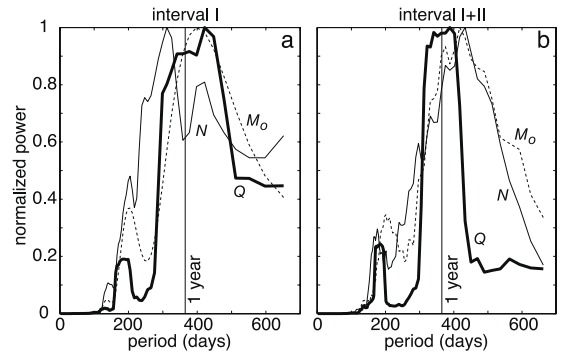

Fig. 5. Period content of time series. Ten-day running average power spectra, normalized by their respective maximum power, of stream discharge, Q (bold solid line), number of earthquakes, N (thin solid line), and seismic moment, M_o (thin dashed line). Dominant periods around one year occur for both interval I (a) and interval I+II (b).

N, and M_o have yearly periodicity, we determine their power spectra which indeed show dominant periods of about one year (Fig. 5) for both intervals I and I+II.

Rather than using monthly binned data averaged over all years from Fig. 4 to determine cross-correlation coefficients, we use the actual time series at a resolution of one day. Seismicity is binned to yield daily number of earthquakes, N, and total daily seismic moment, M_o. Next, we apply moving least-squares polynomial fits (Appendix C) of order ≤ 5 to Q, N, and M_o (Fig. 6), resulting in the interpolated time series denoted $\overline{Q}$, $\overline{N}$, and $\overline{M_o}$, respectively. This type of interpolation ensures that the data are optimally matched in a least-squares sense and that later determination of cross-correlation coefficients between time series is based on equivalent frequency bands. Moreover, interpolation of N and M_o provides evenly spaced data allowing for standard spectral analysis techniques. For better temporal comparison, the interpolated data from Fig. 6 (black curves) are shown normalized by their respective maximum values in Fig. 7.

For a lead channel f and a lag channel g, the normalized cross- ($f \neq g$) and auto- ($f = g$) correlation coefficients, $\Phi_{fg}(t)$, at a time lag of t, are given by:

$$-1 \leq \Phi_{fg}(t) = \frac{\phi_{fg}(t)}{\sqrt{\phi_{ff}(0)}\sqrt{\phi_{gg}(0)}} \leq 1 \qquad (3)$$
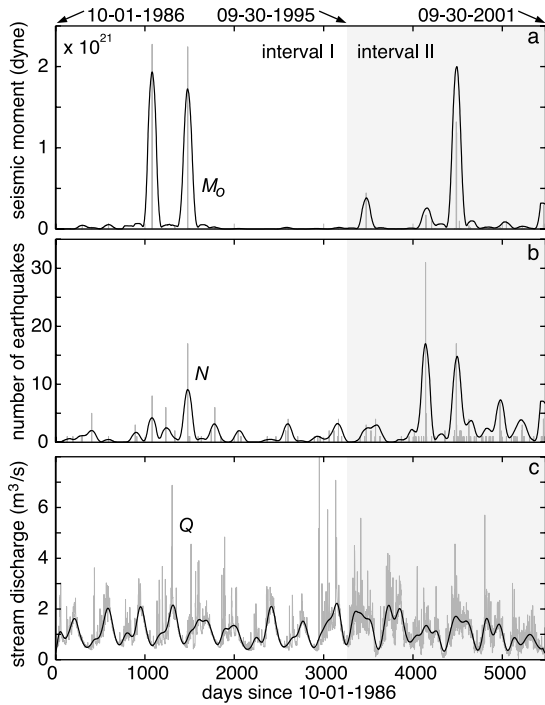
Fig. 6. Original (gray) and interpolated (black) time series of (a) seismic moment, (b) number of earthquakes, and (c) stream discharge of Salmon River at Mt. Hood. Stream discharge includes predicted data from Fig. 3 for interval II. Interpolation is performed using a moving least-squares polynomial fit method of order ≤ 5 per segment as described in the text and in Appendix C. This ensures that the data are optimally matched in a least-squares sense and that the series can be compared at equivalent frequency bands (Fig. 7).

where:

$$\phi_{fg} = \int_{-\infty}^{\infty} f(\tau)\, g(t+\tau)\, \mathrm{d}\tau \qquad (4)$$

The normalization ensures that perfect correlation, no correlation, and perfect anticorrelation are indicated by values of 1, 0, and -1, respectively.

We determine normalized unbiased cross-correlation coefficients, $\Phi_{\overline{QN}}$ and $\Phi_{\overline{QM_\circ}}$ (Fig. 8) for the time series. Cross-correlations show statistically significant peaks at 151 days that are distinct from 99% confidence intervals for random earthquake distributions (Appendix D).

To reduce possible dominance by a year with exceptionally high seismicity, we also determine moving normalized unbiased cross-correlation co-
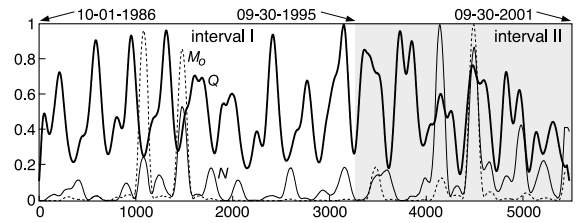

Fig. 7. Interpolated time series from Fig. 6, normalized by each series' absolute maximum value. Local maxima of number of earthquakes (thin solid line) and seismic moment (thin dashed line) typically follow local maxima of stream discharge (bold solid line) after a time lag of about 151 days.

efficients, $\overline{\Phi}_{fg}$, on overlapping segments within each time series (Appendix D). The segment width is 3 years with 30 days shift after each cross-correlation calculation resulting in 75 and 109 segments for intervals I and I+II, respectively. For each segment 20 repetitions are performed so that a total of over 1000 and 2000 iterations are used to determine the confidence intervals for intervals I and I+II, respectively (Appendix D). Fig. 9 shows statistically significant moving cross-correlation coefficients for $\overline{\Phi}_{\overline{QN}}$ and $\overline{\Phi}_{\overline{QM_\circ}}$ that are always distinct from the 90%, and in three quarters of the cases even from the 99%, confidence limits for random earthquake distributions. Results from all segments are averaged for each
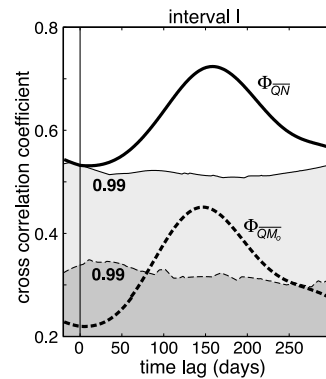
Fig. 8. Time lag versus unbiased normalized cross-correlation coefficients $\Phi_{\overline{QN}}$ (bold solid line) and $\Phi_{\overline{QM_\circ}}$ (bold dashed line) for interval I. Thin horizontal lines indicate the respective upper bounds of the 99% confidence intervals of 1000 cross-correlations for randomly assigned phases for each lag channel (Appendix D). Lower bounds are comparable to the negative of the upper bounds. Both curves suggest a time lag of about 151 days.

Fig. 9. Time lag versus the mean of the unbiased normalized moving cross-correlation coefficients $\overline{\Phi}_{\overline{QN}}$ (bold solid line) and $\overline{\Phi}_{\overline{QM_o}}$ (bold dashed line). Thin horizontal lines 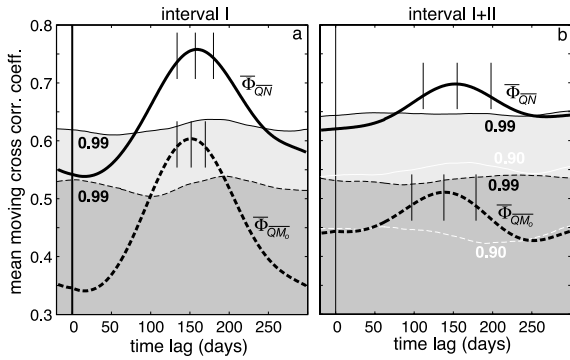indicate the respective upper bounds of the 99% (black) and 90% (white) confidence intervals of over 2000 cross-correlations for randomly assigned phases for each lag channel (Appendix D). Lower bounds are comparable to the negative of the upper bounds. Vertical lines at maximum coefficient values indicate mean (center line) and mean ± 1σ standard deviation (outer lines) for the respective time lags determined from 75 (a) and 109 (b) moving windows of 3-year width. The four mean time lags and respective standard errors are (in days): (a) 157 ± 2.7 (solid line), 152 ± 2.1 (dashed line); (b) 155 ± 4.1 (solid line), 139 ± 3.9 (dashed line), resulting in a total mean and standard error of 151 ± 6.6 days.

time lag (bold lines in Fig. 9). For both $\overline{\Phi}_{\overline{QN}}$ and $\overline{\Phi}_{\overline{QM_o}}$ a maximum is reached for a time lag of about $\Gamma \approx 151$ days.

3. Discussion

In the following we describe processes that can cause hydroseismicity and provide a model that allows us to determine both hydraulic diffusivity, κ, and critical pressure change, P'. From κ we then estimate hydraulic conductivity, K_h, and permeability, k. Throughout the discussion we compare our results with other studies.

3.1. Causes of hydroseismicity

Principal mechanisms involved in triggering hydroseismicity may be explained by combining concepts from linear poroelasticity [25] with the Coulomb failure criterion:

$$\tau_s = \tau_0 + \mu\,\sigma'_n \tag{5}$$

where τ_s, τ_0, μ are the fault's shear strength, cohesion, and coefficient of friction, respectively, and σ'_n is the effective normal stress across the fault. Throughout this paper compressive stresses are positive. σ'_n clamps the fault requiring larger shear stresses, τ, to induce failure (Fig. 10) and is given (Appendix E) by the effective principal stress tensor:

$$\sigma' = \sigma - \alpha P \delta_{ij} \tag{6}$$

where σ is the (regular) principal stress tensor, P is the pore-fluid pressure, δ_{ij} is the Kronecker delta, and α is the Biot–Willis coefficient, defined as:

$$\alpha = 1 - K/K_s \tag{7}$$

Here, K and K_s are the bulk moduli (incompressibilities) of the bulk rock matrix and the solid 'grains', respectively [25]. Deformation can lead to failure, when the shear stress, τ (Appendix E), exceeds the material's shear strength, τ_s, in

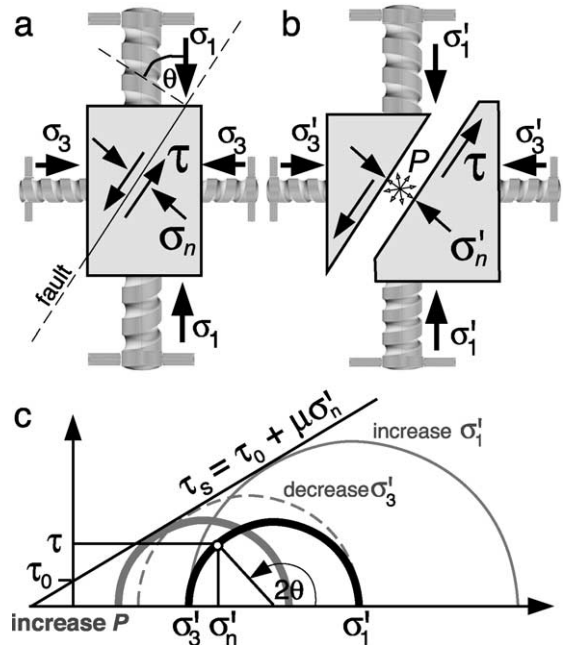Fig. 10. Relationship between stresses: (a) pore-fluid pressure is $P = 0$ so that the effective stress is $\sigma' = \sigma$; (b) pore-fluid pressure is $P \neq 0$ (the fluid-filled gap is drawn only for illustrative purposes) and thus $\sigma' = \sigma - \alpha P \delta_{ij}$ as described in the text; (c) Mohr circle with Mohr–Coulomb failure envelope (diagonal line). For explanation see main text.

Eq. 5, for a given effective normal stress σ'_n. Because σ'_n and τ depend on both orientation of the fault within a stress field and on the magnitude of the stresses (Eqs. E1 and E2), failure can be triggered by changes in both θ and σ' (Fig. 10). The latter mechanism may induce earthquakes by causing: (1) an increase in σ'_1, (2) a decrease in σ'_3, or (3) an equal decrease in all effective principal stresses, for example due to an increase in P (Eq. 6). The first two mechanisms cause failure by increasing the effective differential stress, $\sigma'_1 - \sigma'_3$, and thus shear stress, τ, in Eq. E2. The third mechanism induces failure by decreasing the effective strength of the material caused by a decrease in σ'_n which unclamps the fault and moves the Mohr circle closer to the Mohr–Coulomb failure envelope, while leaving τ unchanged (Fig. 10).

Fluctuations in pore-fluid pressure, P, denoted P', on faults due to an increase in σ'_1 (e.g., by the weight of a filling reservoir that contracts the pore space) occur immediately. In contrast, a local increase in hydrostatic pore-fluid pressure, $P_h = \rho_w g h$, (e.g., by groundwater recharge, reservoir impoundment, or injection of fluids at depth), may trigger earthquakes after a time lag, Γ, that is related to pressure diffusion to the fault. Here, ρ_w is the density of water, g is acceleration due to

Fig. 11. Periodic pore-fluid pressure fluctuations, P'/P_0, at various depths, z (in km), for hydraulic diffusivity $\kappa = 0.3$ m²/s and surface pressure perturbation periodicity $\psi = 1$ year. With increasing depth, the amplitude of the pore-fluid pressure perturbation decreases and the phase lag increases. At a depth of 4.5 km, approximately 10% of the original pressure amplitude, P_0, remains and the delay of the peak is about 151 days (dashed line), i.e., a phase lag of about $0.8\,\pi$.

the Earth's gravity, and h is the height of the water column above the point of interest. Reservoirs exhibit both processes and thus typically cause earthquakes both concurrent with, and delayed from, their filling [2,6]. In this paper we are interested in seismicity induced by groundwater recharge and are thus focusing on earthquakes delayed from recharge by pore-fluid pressure diffusion. Here, the load of the additional groundwater is small and thus triggered seismicity due to a (small) increase in σ'_1 is neglected. Nonetheless, because only the connected pore space is fluid-filled, relatively high hydrostatic pore-fluid pressure changes, P', may be reached that may be sufficient to induce earthquakes.

3.2. Analytic model

We can approximate the effect of seasonal groundwater recharge with periodic yearly ($\psi = 1$ year) pore-fluid pressure variations of amplitude P_0 at the surface ($z = 0$ m) as:

$$P'(t, z = 0) = P_0 \cos\left(\frac{2\pi t}{\psi}\right) \tag{8}$$

Pore-fluid pressure evolution below the water table is governed by the (pressure) diffusion equation. In a one-dimensional half-space the diffusion equation is given by:

$$\kappa \frac{\partial^2 P'}{\partial z^2} = \frac{\mathrm{d}P'}{\mathrm{d}t} \tag{9}$$

where the hydraulic diffusivity:

$$\kappa = \frac{K_h}{S_s} = \frac{gk}{\nu S_s} \tag{10}$$

is assumed constant. Here, K_h, S_s, k, and ν are the hydraulic conductivity, specific storage, permeability, and kinematic viscosity, respectively. The solution to Eq. 9, with the boundary condition given by Eq. 8 is [26]:

$$\frac{P'}{P_0} = \exp\left(-z\sqrt{\frac{\pi}{\psi\kappa}}\right)\cos\left(\frac{2\pi t}{\psi} - z\sqrt{\frac{\pi}{\psi\kappa}}\right) \tag{11}$$

and is graphed in Fig. 11 for $\psi = 1$ year and hydraulic diffusivity $\kappa = 0.3$ m²/s as determined later in Eqs. 13 and 14 for the study region. The exponential term in Eq. 11 describes the decrease in
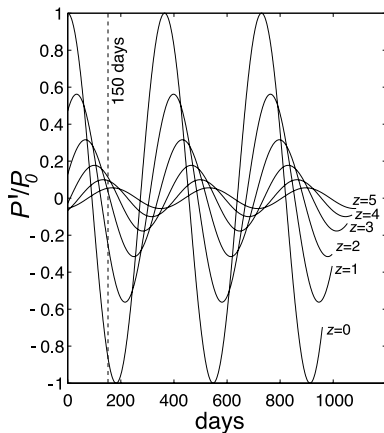
the time-dependent pressure amplitude with depth, z, to $P'/P_0 = 1/e$ at a characteristic length scale (skin depth) of:

$$z_c = \sqrt{\frac{\psi\kappa}{\pi}} \qquad (12)$$

The cosine term in Eq. 11 describes the periodic variations of the pressure signal as a function of both depth, z, and time, t. In addition, both terms in Eq. 11 are a function of κ and ψ.

The actual pore-fluid pressure at depth is $P = P_h + P'$, i.e., the hydrostatic pore-fluid pressure with superimposed periodic pore-fluid pressure fluctuations, P' (Fig. 12). The argument in the cosine in Eq. 11 is expected to be zero (or a multiple of 2π) so that the cosine reaches its maximum, one, during failure (e.g., point C in Fig. 12). It may be reasonable to assume that if a critical pore-fluid pressure, P_c, had been reached before the cosine maximum (e.g., point B in Fig. 12) then failure should have occurred at shallower depths where a cosine maximum reaches the same critical pore-fluid pressure, P_c, earlier in time (e.g., point A in Fig. 12). Here we assume that the subsurface has a pervasive system of at least one fault along which failure can occur at any depth given appropriate stress conditions. Thus, from the condition that the argument of the cosine term in Eq. 11 has to be zero, we can determine κ from:

$$\kappa = \frac{\psi z^2}{4\pi t^2} \qquad (13)$$

3.3. Hydraulic diffusivity

In our case the proposed period of pressure perturbation is $\psi = 1$ year and the time lag, Γ, between groundwater recharge and seismicity at Mt. Hood is $\Gamma = t = 151$ with a standard error of ± 7 days (Fig. 9). Earthquake phase data for earthquake relocation were not readily available. Thus, we could not resolve whether the 1σ standard deviation in the earthquake depth distribution, $z = 4.5 \pm 2$ km (Fig. 1c), reflects error in determining earthquake locations. Hurwitz et al. [27] suggest that ice caps on many Cascade Range volcanoes may restrict recharge on their summits and uppermost flanks and that the water table
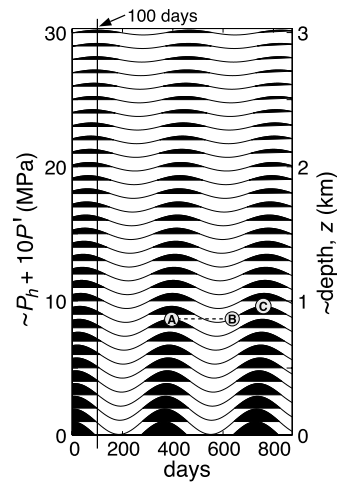

Fig. 12. Hydrostatic pressure, P_h, (at depths from 0 to 3 km) with superimposed (for better visibility) 10-fold exaggerated periodic pore-fluid pressure fluctuations, $P = P_h + 10P'$, versus time for $\kappa = 0.3$ m^2/s and periodicity of $\psi = 1$ year. The critical pore-fluid pressure for failure should be reached at the maximum of the cosine term and a minimum possible depth (point A) as explained in the main text. At a depth of 3 km, the peak of the pressure perturbation is delayed (with respect to the surface) by 100 days (vertical line). Thus, at the mean earthquake depth of about 4.5 km the peak is delayed by the determined time lag of about 151 days. The upper halves of the sinusoids are filled to better visualize the decrease in amplitude and increase in phase lag of the pore-fluid pressure perturbation with increasing depth.

below stratovolcanoes may thus be relatively deep. Consequently, pore-fluid pressure diffusion distances to mean seismic depths may be shorter than the 4.5 km assumed here, while relatively slow flow through the unsaturated zone above the water table could delay fluctuations of water table levels. Furthermore, isotopic contents of water discharged for example at hydrothermal Meadows Spring suggest a recharge elevation of 2700–2900 m, i.e., about 600 m below the summit of Mt. Hood [28]. However, lowering of the water table not only reduces the available diffusion time, t, in the saturated zone but also decreases the diffusion depth, z, to the earthquakes. Lower values of t and z in Eq. 13 tend to cancel each other. In addition, earthquake depths are determined relative to a horizontal plane that is approximately at the mean elevation (~ 1 km) of the relevant seismometers in the region. As a result, z and t assumed here are probably both somewhat

smaller than may be expected. Due to the large uncertainty in earthquake depth (± 2 km) already considered and due to the cancelling effects of reducing both z and t, we neglect the effects of water table reduction by a possible 0.5–1 km relative to the surface.

Using $\psi = 1$ year, $t \approx 151$ days, and $z \approx 4.5$ km in Eq. 13 yields a hydraulic diffusivity of:

$$\kappa = 0.30 \pm 0.22 \ \mathrm{m^2/s} \tag{14}$$

This value of κ agrees with other crustal hydraulic diffusivities compiled by Talwani and Acree [1] and is in the upper range for fractured igneous rocks [29]. Gao et al. [30] suggest a value as high as 1 m²/s for some fractured volcanic systems.

3.4. Critical pore-fluid pressure change

The step-function characteristics of a pore-fluid pressure increase due to initial reservoir impoundment and its error function solution [1,31] do not allow for evaluation of the critical value of P'/P_0 at which failure occurs [1]. In contrast, the additional temporal information provided here by the periodicity of the surface pressure perturbation in the case of seasonal groundwater recharge allows for estimation of critical P'/P_0. Because failure is likely to occur when the cosine term in Eq. 11 is one, we can determine P'/P_0 for the above calculated value of $\kappa = 0.3$ m²/s at a mean depth of about $4 \leq z \leq 4.5$ km and period $\psi = 1$ year as:

$$\frac{P'}{P_0} = \exp\left(-z\sqrt{\frac{\pi}{\psi\kappa}}\right) \approx 0.1 \tag{15}$$

Thus, about 10% of the estimated amplitude of near-surface pressure variations appears to be sufficient to trigger hydroseismicity at Mt. Hood.

Average annual precipitation in the (Oregon) Cascades, and particularly at Mt. Hood, is about 3 m [32] of which approximately 50% infiltrates the ground [33,34] mostly during spring snow melt. This leads to infiltration rates of about 1.5 m/year concentrated during a few months. Lava flows in the region typically have near-surface porosities of about 15% [35] that decrease with depth. Thus, groundwater levels may fluctuate annually by approximately 10 m resulting in seasonal fluid pressure variations that may exceed $P_0 = 0.1$ MPa. Therefore, according to Eq. 15, the critical pore-fluid pressure increase at depth $z \approx 4.5$ km may be as low as $P' \approx 0.01$ MPa, and possibly lower, at Mt. Hood.

While several studies mentioned in Section 1, as well as this paper, suggest that some earthquakes are triggered by pore-fluid pressure perturbations, the necessary critical pore-fluid pressure increase, P', is uncertain [1]. However, it is often argued that many faults are near critically stressed [36]. Therefore, small stress changes invoked by a variety of different mechanisms may be sufficient to cause seismicity on some pre-existing faults. Examples include earthquake triggering by solid Earth and ocean tides [37–39], seasonal modulations of seismicity by the load of snow [40], precipitation- and snow melt-induced seismicity [16,19] and general fluid-driven seismicity [41]. Lockner and Beeler [42] conduct laboratory studies of rock failure along pre-existing faults induced by periodic axial stress changes superimposed on a confining pressure of 50 MPa. They find a transition from weak to strong correlation between periodic stress and failure at an amplitude of 0.05–0.1 MPa shear stress. Roeloffs [6,29] suggests that an increase of $P' \approx 0.1$ MPa can cause reservoir-induced seismicity. Similarly, possible triggering of earthquakes by static stress changes of about 0.1 MPa and less has been proposed by King et al. [43] and Stein et al. [44–46]

Harris [47] summarizes the work of several authors and states that "It appears that static stress changes as low as 0.01 MPa (0.1 bar) can affect the locations of aftershocks".

The examples cited previously as well as our results suggest that the necessary stress change for earthquake initiation on pre-existing faults may be as low as 0.01–0.1 MPa which is only a fraction of the coseismic stress drop. Therefore, Harris [47] points out that Coulomb stress changes are said to 'enhance' the occurrence of an earthquake, as opposed to generating it. We support this view and suggest that pore-fluid pressure changes due to groundwater recharge at Mt. Hood increase the probability of seasonal earthquake occurrences.

Heki [40] states that seasonal seismicity is not

expected if the rate of secular (long-term) regional stress increase is much larger than the annual superimposed disturbance. For the case of the Cascades subduction zone, and assuming the validity of a characteristic earthquake model [48], the annual secular stress increase may be estimated by the (approximately constant) coseismic stress drop, $\Delta\sigma \approx 10$ MPa, divided by the average recurrence interval, $t_r \approx 300$ years, of large earthquakes. Estimated annual pore-fluid pressure fluctuations of 0.01 MPa/year at Mt. Hood at a mean earthquake depth of $z = 4.5$ km are comparable to $\Delta\sigma/t_r \approx 0.03$ MPa/year. Therefore, the pore-fluid pressure fluctuations below Mt. Hood at depths of about 4.5 km caused by groundwater recharge may be large enough to induce seasonal hydroseismicity.

The concentration of (hydro-)seismicity south of Mt. Hood may be due to preferential occurrences of active faults in this region [28,49,50]. Jones and Malone [50] performed earthquake relocations and determined focal mechanisms of events from the June–July 2002 swarm which reveal distinct clusters along normal faults (e.g., White River fault) located south of Mt. Hood as well as events located beneath the summit that appear to be magma-related. This relation between snow melt, groundwater recharge, and seismicity on faults that are kept relatively permeable may also be reflected by the occurrence of the only hydrothermal springs (Swim Warm Springs, Meadows Spring) at Mt. Hood [27,28] in the region south of the volcano (Fig. 1a).

3.5. Hydraulic conductivity and permeability

Once the hydraulic diffusivity, κ, is known, the hydraulic conductivity, K_h, permeability, k, or specific storage, S_s, can be determined by Eq. 10. The specific storage is given by:

$$S_s = \rho g(\alpha + n\beta) \tag{16}$$

where α is the bulk aquifer compressibility (at constant vertical stress and zero lateral strain), n is the pore fraction, and $\beta = 4.8 \times 10^{-10}$ m^2/N is the compressibility of water. If we assume a mean $n \approx 0.05$ for the study region [33] and $\alpha = 10^{-10}$ m^2/N for fractured rock [6,51], then, for the hy-

draulic diffusivity range given in Eq. 14, the hydraulic conductivity is:

$$8 \times 10^{-8} \le K_h = \kappa S_s \le 5 \times 10^{-7} \text{ m/s} \tag{17}$$

which, from Eq. 10 and for a kinematic water viscosity of $\nu \approx 10^{-7}$ m^2/s at 80°C, corresponds to a permeability range of:

$$8 \times 10^{-16} \le k \le 5 \times 10^{-15} \text{ m}^2 \tag{18}$$

for the upper ~ 6 km of the crust at Mt. Hood.

The suggested permeabilities are relatively high compared with a maximum of $k \approx 10^{-16}$ m^2 required for mostly conductive heat transfer [52] as suggested for the Oregon Cascades at depths below about 2 km. However, we suggest two possible arguments that potentially explain why k is higher than may be expected.

First, a reasonable assumption is that permeability is much higher at shallower depths and decreases with depth due to compaction. Therefore, pore-fluid diffusion is much faster in the shallower section and most of the observed time delay probably occurs at deeper portions of the profile. Reducing z for example by a factor of two in Eq. 13 would decrease κ, K_h, and k by a factor of four.

Second, we suggest that the region south of Mt. Hood is anomalous with respect to conductive heat transfer because it hosts the only two hot springs observed on the flanks of Mt. Hood to date [28]. The presence of hot springs suggests that geothermal fluids rise relatively quickly along higher-k paths (e.g., faults) so that time scales for complete conductive thermal equilibration between hot fluids and colder surrounding rock are larger than the travel times of fluids. Indeed, Forster and Smith [21] suggest that hot springs can only be expected for a permeability window of $10^{-17} \le k \le 10^{-15}$ m^2. Our permeability values from Eq. 18 fall in the upper range suggested for hot springs by Forster and Smith [21]. Here, high permeabilities lead to increased water fluxes that result in lower geothermal spring temperatures that are consistent with those (5°C to about 25°C [28]) observed at Meadows Spring and Swim Warm Springs.

The magnitudes for (mostly vertical) permeability, k, calculated here, reflect values for a large

spatial scale that includes Mt. Hood and its near-by active (normal) faults that are kept permeable by rupture and appear to provide fluid pathways. That the magnitudes of hydraulic diffusivity, κ, and permeability, k, are plausible further supports the hypothesis of seasonal elevated seismicity levels due to groundwater recharge in this region.

4. Conclusions

Several arguments support the hypothesis that some seismicity at Mt. Hood, Oregon, is triggered by pore-fluid pressure diffusion as a result of rapid groundwater recharge due to seasonal snow melt. Statistically significant cross-correlation coefficients between groundwater recharge and seismicity suggest a time lag of about 151 days. The values of the correlation coefficients are distinct from those for random temporal earthquake distributions determined by Monte Carlo simulations. The time lag and mean earthquake depth provide a reasonable (mostly) vertical hydraulic diffusivity ($\kappa \approx 10^{-1}$ m^2/s), hydraulic conductivity ($K_h \approx 10^{-7}$ m/s), and permeability ($k \approx 10^{-15}$ m^2) that agree with other studies [1,21,36]. Finally, we determine the critical fraction ($P'/P_0 = 0.1$) of the periodic near-surface pore-fluid pressure fluctuations ($P_0 \approx 0.1$ MPa) that reach the mean earthquake depth, suggesting that $P' \approx 0.01$ MPa can trigger seismicity. This value of $P' \approx 0.01$ MPa is at the lower end of the range of critical pore-fluid pressure changes of $0.01 \leq P' \leq 0.1$ MPa suggested in previous studies [6,29,43,47]. Therefore, while seismicity is distributed throughout the year at Mt. Hood, we conclude that some earthquakes are hydrologically induced by a reduction in effective stress due to a seasonal increase in hydrostatic pore-fluid pressure, P_h, by a small amount P'. In fact, elevated seismicity levels due to such small effective stress changes suggest that the state of stress in the crust at Mt. Hood, Oregon, could be near critical for failure.

Acknowledgements

Appendix A. Seismometer information

The information in Table A1 about the short-period vertical-motion seismometers in the vicinity of Mt. Hood was provided by the Pacific Northwest Seismograph Network. The date column refers to the seismometer installation date.

Appendix B. Box–Jenkins method

The stream discharge of Salmon River is predicted beyond its last measurement by employing a transfer function between Hood River and Salmon River. The transfer function is determined using a Box–Jenkins [23] method. In the case of a single input channel, X_t, investigated here, the output (or lag) channel, Y_t, can depend on both current ($t = 0$) and previous ($t < 0$) input, X_t, as well as on previous output, Y_t. Thus, input and output are related by:

$$Y_t = \frac{\omega(B)}{\delta(B)}X_{t-b} + N_t \tag{B1}$$

where:

$$\frac{\omega(B)}{\delta(B)} = \frac{\omega_0 + \omega_1 B + \omega_2 B^2 + \ldots + \omega_n B^{\eta}}{\delta_0 + \delta_1 B + \delta_2 B^2 + \ldots + \delta_n B^{\gamma}} \tag{B2}$$

Table A1
Seismometer locations and installation dates

Key	Latitude	Longitude	Elevation (km)	Date (mm/yy)
KMO	45°38′07.80″	−123°29′22.20″	0.975	09/82
SSO	44°51′21.60″	−122°27′37.80″	1.242	09/91
TDH	44°17′23.40″	−121°47′25.20″	1.541	09/82
VBE	45°03′37.20″	−121°35′12.60″	1.544	10/79
VCR	44°58′58.18″	−120°59′17.35″	1.015	08/83
VFP	45°19′05.00″	−121°27′54.30″	1.716	10/80
VG2	45°09′20.00″	−122°16′15.00″	0.823	09/85
VGB	45°30′56.40″	−120°46′39.00″	0.729	04/80
VLL	45°27′48.00″	−121°40′45.00″	1.195	10/80
VLM	45°32′18.60″	−122°02′21.00″	1.150	06/80
PGO	45°27′42.60″	−122°27′11.50″	0.253	06/82
AUG	45°44′10.00″	−121°40′50.00″	0.865	10/81
GUL	45°55′27.00″	−121°35′44.00″	1.189	07/86
MTM	46°01′31.80″	−122°12′42.00″	1.121	03/80

is the transfer function with coefficients ω and δ. Because coefficients in ω act on current and previous input and coefficients in γ act on previous output, they may be denoted as moving average (MA) and auto-regressive (AR) processes and the transfer function as a so-called ARMA model. In the previous equations, t is a time index, B is the backshift operator such that $B^b X_t = X_{t-b}$, η and γ are the number of delays for input and output, respectively, and N_t is noise assumed unrelated to the input. Therefore, if the noise, N_t, is neglected and (in our case) $\eta = 4$ and $\gamma = 1$ is selected then the output, Y_t, at time t is given by:

$$\delta_0 Y_t = \delta_1 Y_{t-1} + \omega_0 X_t + \omega_1 X_{t-1} + \omega_2 X_{t-2}$$

$$+ \omega_3 X_{t-3} + \omega_4 X_{t-4} \tag{B3}$$

where $\delta_0 = 1$ is commonly assumed (or else Eq. B3 is divided by δ_0). Therefore, in this example, the current output depends on one ($b = 1$) previous output (Salmon River discharge) as well as on the current ($b = 0$) and previous four ($1 \leq b \leq 4$) inputs (Hood River discharge).

Appendix C. Moving polynomial interpolation

The daily binned seismic data have to be interpolated so that continuous time series are obtained on which standard spectral analyses can be performed. We apply a moving polynomial interpolation, rather than convolution of the data with a Gaussian normal curve, so that no artificial frequency is introduced by a convolution kernel. In addition, the moving polynomial approach allows interpolation with low-order (≤ 5) polynomials while ensuring that the data are optimally matched in a least-squares sense. For all three series, Q, N, and M_o, the width of the moving window is 1/12th of the total series length and the step width is 1/10th of the window width. The polynomial coefficients, m_{LS}, are found using the standard least-squares solution from inverse theory given as $m_{LS} = [G^T G]^{-1} G^T d$, where G is the (up to) fifth-order polynomial model matrix and d is the data vector. Multiple interpolation values for a given time step result from the overlap of the moving window and are averaged.

Appendix D. Correlation coefficients

We determine auto- ($f = g$) and cross- ($f \neq g$) correlation coefficients for time series f and g as described in principle by Eqs. 3 and 4. In practice, correlation coefficients, ϕ_{fg}, for positive time lags, l, are calculated by:

$$\phi_{fg}(l) = \frac{1}{M-l} \sum_{m=0}^{M-l-1} f_{m+l} g_m \tag{D1}$$

where m and M are the index and the length of the (zero-padded) time series, respectively. Dividing by $(M-l)$ provides so-called unbiased cross-correlations where the reduced overlap length of the series for large time lags is accounted for. Correlation coefficients are then normalized as described by Eq. 3.

We determine confidence intervals for the case where one of the two time series is assigned random phases for each frequency so that its auto-correlation is unaffected. Typically 500 iterations (each assigning new random phases for each frequency) of cross-correlations, $\phi_{fg}(t)$, at lag t, are performed by spectral multiplication directly in the frequency domain as:

$$\phi_{fg}(t) = F^{-1}\{F\{f\}F^*\{g\}\} \tag{D2}$$

where F, F^{-1}, and F^* denote the Fourier transform, its inverse, and its complex conjugate, respectively. The range of values that contain 90% of the data for a given time lag is the 90% confidence interval for that time lag.

To reduce the effect of years with unusually high seismicity, moving cross-correlation coefficients within overlapping subsections (windows) of the time series are also determined. Here, based on all windows that provide output for a given time lag, the mean coefficient per time lag is determined. Each window has to be short enough so that the years with dominant seismicity do not fall in all windows but large enough so that cross-correlations are performed over several periods (we chose 3 years). Furthermore, the time lags of coefficients that are distinct from the confidence interval for random phase distributions are used to calculate a mean and a standard deviation for the (positive) time lag around the first local maximum coefficient.

Appendix E. Normal and shear stresses

The effective normal stress, σ'_n, is given by:

$$\sigma'_n = \frac{\sigma'_1 + \sigma'_3}{2} + \frac{\sigma'_1 - \sigma'_3}{2}\cos(2\theta) \tag{E1}$$

where σ'_1 and σ'_3 are the effective principal maximum and minimum compressive stresses, respec-

tively, and θ is the angle between σ'_1 and the normal to the failure plane (Fig. 10a). The shear stress, τ, is given by:

$$\tau = \left|\frac{\sigma'_1 - \sigma'_3}{2}\sin(2\theta)\right| \tag{E2}$$

References

[1] P. Talwani, S. Acree, Pore pressure diffusion and the mechanism of reservoir-induced seismicity, PAGEOPH 122 (1984/85) 947–965.

[2] D.W. Simpson, W.S. Leith, C.H. Scholz, Two types of reservoir-induced seismicity, Bull. Seismol. Soc. Am. 78 (1988) 2025–2040.

[3] H.K. Gupta, Reservoir-Induced Earthquakes, Elsevier, New York, 1992, 364 pp.

[4] C.B. Raleigh, J.H. Healy, J.D. Bredehoeft, Faulting and crustal stress at Rangely, Colorado, in: Flow and Fracture of Rocks, Geophys. Monogr. Ser., 1972, pp. 275–284.

[5] C.B. Raleigh, J.H. Healy, J.D. Bredehoeft, An experiment in earthquake control at Rangely, Colorado, Science 191 (1976) 1230–1237.

[6] E.A. Roeloffs, Fault stability changes induced beneath a reservoir with cyclic variations in water level, J. Geophys. Res. 93 (1988) 2107–2124.

[7] J.H. Healy, W.W. Rubey, D.T. Griggs, C.B. Raleigh, The Denver earthquakes, Science 161 (1968) 1301–1310.

[8] P.A. Hsieh, J.D. Bredehoeft, A reservoir analysis of the Denver earthquakes: A case of induced seismicity, J. Geophys. Res. 86 (1981) 903–920.

[9] P. Segall, Stress and subsidence resulting from subsurface fluid withdrawal in the epicentral region of the 1983 Coalinga Earthquake, J. Geophys. Res. 90 (1985) 6801–6816.

[10] P. Segall, Earthquakes triggered by fluid extraction, Geology 17 (1989) 942–946.

[11] M.D. Zoback, J.C. Zinke, Production-induced normal faulting in the Valhall and Ekofisk oil fields, Pure Appl. Geophys. 159 (2002) 403–420.

[12] A. Nur, J.R. Booker, Aftershocks caused by pore fluid flow?, Science 175 (1972) 885–887.

[13] K.W. Hudnut, L. Seeber, J. Pacheco, Cross-fault triggering in the November 1987 Superstition Hills earthquake sequence, southern California, Geophys. Res. Lett. 16 (1989) 199–202.

[14] J.K. Costain, G.A. Bollinger, J.A. Speer, Hydroseismicity: A hypothesis for the role of water in the generation of intraplate seismicity, Seismol. Res. Lett. 58 (1987) 41–64.

[15] P. Roth, N. Pavoni, N. Deichmann, Seismotectonics of the eastern Swiss Alps and evidence for precipitation-induced variations of seismic activity, Tectonophysics 207 (1992) 183–197.

[16] L.W. Wolf, C.A. Rowe, R.B. Horner, Periodic seismicity near Mt. Ogden on the Alaska-British Columbia border:

A case for hydrologically triggered earthquakes?, Bull. Seismol. Soc. Am. 87 (1997) 1473–1483.

[17] M.-J. Jiménez, M. García-Fernández, Occurrence of shallow earthquakes following periods of intense rainfall in Tenerife, Canary Islands, J. Volcanol. Geotherm. Res. 103 (2000) 463–468.

[18] H. Ogasawara, K. Fujimori, N. Koizumi, N. Hirano, S. Fujiwara, S. Otsuka, S. Nakao, K. Nishigami, K. Taniguchi, Y. Iio, R. Nishida, K. Oike, Y. Tanaka, Microseismicity induced by heavy rainfall around flooded vertical ore veins, PAGEOPH 159 (2002) 91–109.

[19] V. Léonardi, F. Arthaud, A. Tovmassian, A. Karakhanian, Tectonic and seismic conditions for changes in spring discharge along the Garni right lateral strike slip fault (Armenian upland), Geodin. Acta 11 (1998) 85–103.

[20] M.D. Zoback, J.H. Healy, Friction, faulting, and in-situ stress, Ann. Geophys. 2 (1984) 689–698.

[21] C. Forster, L. Smith, The influence of groundwater flow on thermal regimes in mountainous terrain: A model study, J. Geophys. Res. 94 (1989) 9439–9451.

[22] M. Manga, Hydrology of spring-dominated streams in the Oregon Cascades, Water Resour. Res. 32 (1996) 2435–2439.

[23] G.E.P Box, G.M. Jenkins, G.C. Reinsel, Time Series Analysis: Forecasting and Control, Prentice-Hall, Englewood Cliffs, NJ, 1994, 598 pp.

[24] T. Lay, T.C. Wallace, Modern Global Seismology, Academic Press, London, 1995, 521 pp.

[25] H.F. Wang, Theory of Linear Poroelasticity, Princeton University Press, Princeton, NJ, 2000, 287 pp.

[26] D.L. Turcotte, G. Schubert, Geodynamics, Cambdridge University Press, Cambridge, 2002, 456 pp.

[27] S. Hurwitz, K.L. Kipp, S.E. Ingebritsen, Groundwater flow, heat transport, and water-table position within volcanic edifices: Implications for volcanic processes in the Cascade Range, J. Geophys. Res., 2003 (in press).

[28] M. Nathenson, Springs on and in the vicinity of Mount Hood, Oregon, USGS Open-File Report, 2003 (in review).

[29] E. Roeloffs, Poroelastic techniques in the study of earthquake-related hydrologic phenomena, Adv. Geophys. 37 (1996) 135–195.

[30] S.S. Gao, P.G. Silver, A.T. Linde, I.S. Sacks, Annual modulation of triggered seismicity following the 1992 Landers earthquake in California, Nature 406 (2000) 500–504.

[31] H.S. Carslaw, J.C. Jaeger, Conduction of Heat in Solids, Clarendon Press, Oxford, 1959, 510 pp.

[32] Spatial Climate Analysis Service, Average annual precipitation of Oregon, Oregon State University, online, 2002.

[33] S.E. Ingebritsen, D.R. Sherrod, R.H. Mariner, Rates and patterns of groundwater flow in the Cascade Range Volcanic Arc, and the effect of subsurface temperatures, J. Geophys. Res. 97 (1992) 4599–4627.

[34] M. Manga, A model for discharge in spring-dominated streams and implications for the transmissivity and recharge of Quaternary volcanics in the Oregon Cascades, Water Resour. Res. 33 (1997) 1813–1822.

[35] S.E. Ingebritsen, R.H. Mariner, D.R. Sherrod, Hydrothermal Systems of the Cascades Range, North-central Oregon, U.S. Geol. Surv. Prof. Pap. 1044-L, 1994.

[36] J. Townend, M.D. Zoback, How faulting keeps the crust strong, Geology 28 (2000) 399–402.

[37] S. Tanaka, M. Ohtake, H. Sato, Spatio-temporal variation of the tidal triggering effect on earthquake occurrence associated with the 1982 South Tonga earthquake of Mw 7.5, Geophys. Res. Lett. 29 (2002) art. no. 1756.

[38] W.S.D. Wilcock, Tidal triggering of micro earthquakes on the Juan de Fuca Ridge, Geophys. Res. Lett. 28 (2001) 3999–4002.

[39] J. Kasahara, Tides, earthquakes, and volcanoes, Science 297 (2002) 348–349.

[40] K. Heki, Snow load and seasonal variation of earthquake occurrence in Japan, Earth Planet. Sci. Lett. 207 (2003) 159–164.

[41] L. Audin, J.-P. Avouac, M. Flouzat, J.-L. Plantet, Fluid-driven seismicity in a stable tectonic context: The Remiremont fault zone, Vosges, France, Geophys. Res. Lett. 29 (2002) art. no. 1091.

[42] D.A. Lockner, N.M. Beeler, Premonitory slip and tidal triggering of earthquakes, J. Geophys. Res. 104 (1999) 20133–20151.

[43] G.C.P. King, R.S. Stein, J. Lin, Static stress changes and the triggering of earthquakes, Bull. Seismol. Soc. Am. 84 (1994) 935–953.

[44] R.S. Stein, G.C.P. King, J. Lin, Change in failure stress on the southern San Andreas Fault system caused by the 1992 magnitude = 7.4 Landers earthquake, Science 258 (1992) 1328–1332.

[45] R.S. Stein, G.C.P. King, J. Lin, Stress triggering of the 1994 m = 6.7 Northridge, California, earthquake by its predecessors, Science 265 (1994) 1432–1435.

[46] R.S. Stein, The role of stress transfer in earthquake occurrence, Nature 402 (1999) 605–609.

[47] R.A. Harris, Introduction to special section: Stress triggers, stress shadows, and implications for seismic hazard, J. Geophys. Res. 103 (1998) 24347–24358.

[48] K. Shimazaki, T. Nakata, Time-predictable recurrence model for large earthquakes, Geophys. Res. Lett. 7 (1980) 279–282.

[49] C.S. Weaver, R.D. Norris, C. Trisler-Jonientz, Results of seismological monitoring in the Cascades Range 1962–1989: Earthquakes, eruptions, avalanches, and other curiosities, Geosci. Can. 17 (1990) 158–162.

[50] J. Jones, S.D. Malone, Mount Hood earthquake activity: Volcanic or tectonic origins (Abstract)?, EOS Trans. AGU 83 (Fall Meet. Suppl. 12A) (2002) 1179.

[51] P.A. Domenico, F.W. Schwartz, Physical and Chemical Hydrogeology, Wiley, New York, 1998, 506 pp.

[52] C.E. Manning, S.E. Ingebritsen, Permeability of the continental crust: Implications of geothermal data and metamorphic systems, Rev. Geophys. 37 (1999) 127–150.